Contents lists available at ScienceDirect

Corrosion Science

Corrosion of 316L exposed to highly concentrated borated water used as shield in nuclear fusion experimental reactors cooling circuits

C. Gasparrini [a,b,*], J.O. Douglas [c], A. Yazdanpanah [d], R. Stroud [c], G. Divitini [e], M. Dabalà [d],
G.G. Scatigno [f], S. Pedrazzini [c,1], M.R. Wenman [b], D. Badocco [g], P. Pastore [g], N. Terranova [h],
G. Mariano [h], F. Dacquait [i], M. Dalla Palma [a,j], R. Villari [i], P. Sonato [a,d]

[a] Consorzio RFX, Corso Stati Uniti 4, Padua 35127, Italy
[b] Department of Materials & Centre for Nuclear Engineering, Imperial College London, London SW7 2AZ, UK
[c] Department of Materials, Imperial College, South Kensington Campus, London SW7 2AZ, UK
[d] Department of Industrial Engineering, University of Padova, Via Marzolo 9, Padua 35131, Italy
[e] Istituto Italiano di Tecnologia, via Morego 30, Genoa 16163, Italy
[f] EDF, Barnwood, Gloucester GL4 3RS, UK
[g] Department of Chemical Sciences, University of Padova, Padua 35131, Italy
[h] FSN Department, ENEA, C. R. Frascati, Frascati 00044, Italy
[i] CEA, DES, IRESNE, DTN, Saint-Paul Lez Durance F-13108, France
[j] CNR, ISTP, Institute for Plasma Science and Technology, Padua, Italy

ARTICLE INFO

ABSTRACT

Borated water is used as a shield in nuclear fusion cooling circuits. General corrosion, activated corrosion products (ACPs) formation and stress corrosion cracking initiation of 316 L steels exposed to ultrapure water (UPW) or 8000 ppm B water at 80 °C were tested. A Ni enriched sub-oxide layer, a transition layer and oxide layer were observed using advanced characterisation (STEM-EELS, APT). The oxide formed in UPW was protective (Cr:O 40:45), the oxide formed in 8000 ppm B was non-passivating. 8000 ppm B led to higher release of Fe, Cr and Mo, 316 L was more prone to SCC initiation and enhanced ACPs formation.

1. Introduction

Satisfying the world's ever-increasing demand for low carbon, secure and affordable electricity and energy is one of the greatest challenges of this century [1]. Nuclear fusion is aiming to join the family of non-greenhouse gas emitting electricity sources, currently consisting of renewables and nuclear fission power plants. Nuclear fusion [2] is attracting a wide and renewed interest gaining funding and media attention from the public and private sectors in recent years [3]. For the realisation of the first fusion reactor power plant multiple challenges are, however, yet to be solved. Some of the main materials science challenges yet to be addressed are:

- construction of a breeding blanket module for tritium self-sufficiency [4],
- realisation of a component able to perform as a reactor power heat exhaust (divertor) [5],
- construction of a fusion-tailored neutron irradiation facility to test materials able to survive exposure to highly energetic neutrons generated in a fusion power plant [6].

To overcome each challenge, the fusion community is planning to build and operate a dedicated international facility in parallel to the construction of ITER. ITER should be the first reactor to demonstrate the possibility to produce net energy from nuclear fusion reactions. ITER will not produce any electricity as it will serve as a testbed for many of the components required for the first prototype/pilot fusion power plant

which, in Europe, is the so-called demonstrator plant (DEMO) [7]. From the successful operation of the first of a kind demonstrator plant, DEMO, to a commercial fusion power plant other technical challenges will, however, need to be overcome.

To address the technological challenge of a reliable heat power exhaust for DEMO, a facility called Divertor Tokamak Test (DTT) facility [8–10] is going to be built in Frascati, Rome, Italy. This experimental reactor shares some common features with other fusion research reactors built internationally, such as Japan Torus-60 Super Advanced (JT60-SA) [11] and Korea Superconducting Tokamak Advanced Research (KSTAR) [12]. One of the common characteristics of these three experimental nuclear fusion reactor cooling circuits is the use of borated water flowing in the water cooling circuit in their vacuum vessel. Cooling circuits in nuclear fusion experimental reactors like ITER [13–15] and ITER facilities [16,17] will operate with water. DTT, KSTAR and JT60SA will exploit water with boric acid to shield the superconducting magnets from neutron irradiation [18]. Neutron shielding is achieved with the use of highly concentrated, highly enriched boric acid dissolved in water flowing within the double shell walls of the vacuum vessel steel structure. Adding boric acid in the water cooling circuit is a feature shared with nuclear fission power plants, namely pressurized water reactors (PWRs) [19]. Boric acid naturally contains approximately 19.8% ^{10}B [11], PWRs generally operate with natural boric acid [20]; an enriched boric acid (EBA) regime using up to 40% in ^{10}B is being pursued in some plants to reduce the amount of H_3BO_3 that needs to be added into the water and reduce the amount of LiOH (99.95% enriched in ^{7}Li) to reach the desired pH_T between 6.9 and 7.4 at 300 °C [19], French PWRs aim for a pH_T=7.2. The DTT requirement considers 8000 ppm B with 95% ^{10}B [18] without addition of LiOH, which brings the water to pH < 3.7 at 60 °C [21,22].

Stainless steels have been used extensively in the nuclear industry ensuring the reliable operation of nuclear power plants for 60+ years. However, 316 L type stainless steels are not immune to phenomena such as corrosion [23,24] and stress corrosion cracking (SCC) [13,25−27] especially at low pH [26]. The water pH chosen in nuclear fusion research reactors is challenging compared to the one used in the current power plant fission fleet given the higher concentration of boric acid used (8000 ppm B in DTT, 13,400 ppm B in KSTAR and JT60SA [22] vs ≤ 2400 ppm B in PWRs). Very recent issues of SCC in 316 L in the current nuclear fission power plant fleet [28] and in ITER key components [29] highlight the importance of choosing and maintaining an optimum environment and choosing an appropriate water chemistry.

In this work, corrosion of 316 L type stainless steels exposed to the DTT vacuum vessel (VV) borated water was investigated. General corrosion of 316 L base metal and welds were tested using metal release experiments in stagnant conditions [30]. Stagnant conditions were used given that water flowing in the DTT VV has a maximum velocity of 0.5 m/s at inlet, otherwise it generally flows <0.01 m/s by design [31]. Release rates and corrosion rates measured from the experiments were used to estimate the amount of activated corrosion products (ACPs) [22] produced during DTT operation in a foreseen neutronic operation scenario [18]. The simulation code used to monitor the formation and redeposition of ACPs in the DTT cooling circuit was OSCAR-Fusion v1.3 [32–34].

To understand the corrosion of 316 L in highly concentrated borated water, the passivating oxide layer formed on samples was characterised by high-resolution microscopy techniques [35] evidencing the role of the passivating oxide layer in steels corrosion. Atomic scale characterisation of the passivating oxide layer chemistry was conducted with atom probe tomography (APT) and transmission electron microscopy (TEM) coupled with electron energy loss spectroscopy (EELS) and energy-dispersed X-ray spectroscopy (EDX). To assess the tendency of 316 L to SCC [36] in highly concentrated borated water compared to pure water, SCC initiation tests using a microcapillary electrochemical test method [37] was used. During the past decades, various electrochemical polarization experiments have been developed for SCC risk

assessment during the crack propagation stage by virtue of direct measurement of the variations in potential and/or current density passing through the test setup [38,39]. However, it is well known that the most time-consuming stage of SCC occurrence is related to the incubation/initiation stage, which could substantially affect the overall life cycle of critical components. As a consequence of extremely localized sites in which SCC initiates, and the difficulties in the detection of such local sites, common electrochemical techniques cannot always provide adequate information. Thus, most of the research in this field is concentrated on crack growth rate determination using pre-cracked standard specimens [38]. Furthermore, for the past 50 years it has been known that the standard test method ASTM G36 in boiling saturated magnesium chloride solution could provide misleading information as a result of significant differences in chloride contamination level compared to actual working environments, and therefore could not be utilized for in-depth analysis of the initial stage of SCC formation [40]. In the authors' previous investigations, microcapillary method for SCC initiation studies proved to be a powerful and highly sensitive technique for the comparative study of SCC initiation risk assessment for stainless steels and nickel-based super alloys [37,41,42], highlighting the possibility of a comprehensive study of the native oxide layer alterations under various conditions. NaCl solution was here used to accelerate the detrimental effect of corrosion due to the presence of Cl- ions, known to be detrimental in SCC of 316 L [36,43].

2. Experimental

316 L steel samples and tungsten inert gas (TIG) welds were provided by Westinghouse - Mangiarotti S.p.A., Monfalcone (GO), Italy. TIG welds were manufactured according to ITER VV requirements, and the ferrite content in base metal vs TIG welds was previously characterised in Gasparrini et al. [30]. Metal release experiments were performed on samples ground with 1200 grit SiC paper in accordance with previous literature on the topic [44–46]. The experimental set up was described in Gasparrini et al. [30]; best practice was used for handling ultra-high purity water [47]. Samples tested had dimensions of 12 mm × 10 mm × 1 mm and were submerged in a 30 mL solution. Ultrapure water was taken from an ad hoc in-house purification system based at Consorzio RFX. High purity acids (trace elemental impurities: Fe < 0.5 ppb, Mn, Mo, Ni, Co, Cr all < 0.1 ppb), SuperPure (SpA) quality purchased from Romil Ltd. (Romil Ltd., The source, Covent drive, Waterbeach, Cambridge, U.K.), were used to minimise metal cross contamination. PFA vessels used for metal release tests [48] were inserted in an environmental chamber at 80 °C in air. Sampling of the water in contact with samples was performed after 3 h, 24 h, 7 days, 3 weeks, 7 weeks and 12 weeks exposure. Fresh solution was inserted in the vessel after each sampling. Water was here referred to as UPW referring to water quality [49]: at production site it fulfilled UPW requirements, solutions were handled in air though, so gaseous contamination cannot be avoided. There was no monitoring on oxygen contamination, though the same solution was used for each set of experiments and vessels were tested at the same time so experimental conditions are considered consistent throughout the experiments. Trace metal analysis was performed using an inductively coupled plasma-mass spectrometry (ICP-MS) using an Agilent Technologies 7700x system (Agilent Technologies International, Santa Clara, CA, USA) [24]. Samples in triplicate and a background control (blank solution) were exposed in different PFA jars. From each jar, two water samples were taken, meaning that each release datapoint represents six independent measurements. The values reported are the average and standard deviations of the six measurements.

Microcapillary SCC initiation studies were performed according to [37] where the solution used was 3.5% sodium chloride solution in distilled and deionized water. The solution was bubbled with high-purity argon gas for 15 minutes prior to the experiments to achieve consistent oxygen levels for all experiments (as a result of the self-controlled environment of the microcapillary method). The

capillary diameter of 500 μm was used implementing the standard three-electrode electrochemical technique with the specimen as the working electrode, platinum wire with a diameter of 0.3 mm and the distance with the specimen surface of 3 mm as the counter electrode, and the standard calomel electrode (SCE) as the reference electrode. All electrochemical experiments were performed utilizing an AMEL 2549 potentiostat at room temperature. Potentiodynamic polarization experiments were performed as the starting point for in-depth analysis of the native oxide layer behaviour and galvanostatic measurements assessed the resistance of the passive layer at a constant current density of 10% higher than the breakdown current density over time of polarization. All electrochemical experiments were performed both without external straining and constant straining in uniaxial tension to 10% higher than yield strength, indicated as 0.2% proof stress, for in-depth SCC initiation risk assessment. Further details regarding the experimental setup could be found in authors' previous publications [37].

XRD analyses were performed on polished samples, ground samples prior and after passivation experiments using a Panalytical X'Pert 3 powder (Malvern Panalytical, Malvern, U.K.). Characterisation of the passive oxide layer on 316 L steels growth after passivation experiments was performed using scanning TEM (STEM) acquiring the High-Angle Annular Dark Field signal (HAADF), coupled with Energy-dispersive X-ray spectroscopy (EDX) and electron energy loss spectroscopy (EELS) using a Thermofisher Spectra 300 with Dual-X, 1.7 sr solid angle of collection operated at 300 kV accelerating voltage. EDX maps were performed on this state-of-the-art system using best practices: ~500 pA current, drift corrected rapid raster acquisition, 1 second/frame, 880 frames. Unlike what is often done in the literature, post- processing was kept to a minimum in order to preserve the quality of the data (no smoothing, full range of values being displayed to show spurious signal and noise level). EELS was performed using a Gatan Continuum with a CMOS-based camera, beam current 500 pA, 20 ms/pixel, dispersion 0.3 eV/ch on focused ion beam (FIB) TEM lamellae. The FIB used was a Thermofisher scientific Helios NanoLab™ 600 and a Thermofisher Helios 5 both equipped with Ga ion source. FIB thinning was performed minimising Ga FIB damage according to best practice[50,51]. Atom probe tomography was conducted with a LEAP 5000 XR, in laser mode. Samples were coated with cobalt on the outer surface to preserve the oxidised/corroded layer. Cobalt was selected as it was not part of the alloy or the electrochemical experimental set-up, making it easy to identify. Wedge-shaped samples were then lifted out using a Thermofisher Helios and mounted on standard Cameca 22-tip silicon coupons using Pt welds. Samples were sharpened to <100 nm diameter before being inserted in the LEAP 5000 XR. APT analysis was performed in laser mode, with an energy of 50 pJ, four samples were made and two of these for each specimen were tested at the same condition. More information can be found in the Appendix.

Simulations with OSCAR-Fusion v1.3 code were performed inputting preliminary thermal hydraulic information of the DTT vacuum vessel cooling circuit. The simulations do not intend to be exhaustive and accurate from a radioprotection point of view given that DTT cooling circuit is not yet finalised nor it is built and approximations had to be inevitably considered in the cooling circuit design and neutronics scenarios. The details of materials in the cooling circuit inputted in the model are shown in Table 1:

Thermofluid-dynamics parameters considered for ACPs calculations reflect the latest information related to the conceptual design of the DTT VV cooling circuit. Nuclear reaction rates for ACPs calculations were based on the work of Villari et al. [18]. The aim of ACPs simulations here presented intend to show the key role of corrosion rates on ACP formation, the results are not intended to be used for radioprotection purposes.

3. Results and discussions

XRD analyses on 316 L base samples after polishing revealed the presence of the austenitic phase (identified with PDF code 96–900–8470). XRD on TIG welds after polishing revealed the presence of two phases: the austenitic phase and a secondary ferritic/martensitic phase; the austenitic phase showing some texturing, with higher peak alongside [0 2 2] compared to [1 1 1]. The presence of a secondary ferritic/martensitic phase in the polished TIG weld samples confirmed the presence of a much greater percentage of δ-ferrite in the weld compared to the base metal, in Gasparrini et al. [30] it was estimated ~11% of ferrite in the TIG weld compared to ~2.9% in the 316 L base metal.

Samples surfaces were prepared using a grinding procedure with a #1200 SiC grit prior to being exposed to water solutions for metal release experiments. This degree of grinding was performed to be consistent with previous literature on the topic [45,52]. Fig. 1 shows the surface morphology of the ground samples analysed by SEM and XRD. Fig. 1e shows XRD analyses on 316 L base metal samples after either polishing or grinding. XRD on the ground samples revealed the presence of two phases: the main austenitic phase and a secondary ferritic/martensitic phase (identified with PDF code 98–006–4795). The ferritic/martensitic phase observed by XRD was related to a martensitic deformed layer induced by the grinding procedure on stainless steel [53]. Grinding effects on the surface were visible by visual inspection and SEM analyses (scratches), see Fig. 1a.

The deformed layer was observed by STEM analysis on samples manufactured by FIB from the top surface, with a thickness of roughly 200–600 nm. Metal release experiments were conducted on ground 316 L base, 316 LN-IG and TIG welds samples.

Fig. 2 summarises the results of metal release experiments performed to assess general corrosion of 316 L base metals and TIG welds during the 12-weeks exposure. By comparing releases of samples exposed to UPW (see definition of UPW in the materials and methods section) and borated water a larger metal release of Fe, Cr and Mo in the 8000 ppm B solution was observed when compared to UPW. Larger releases of Fe, Cr and Mo from 316 L base metals could be a result of the poorer passivating properties of the oxide layer formed in highly concentrated borated water solution compared to UPW. From PWR experience it is known that the protective oxide growth on stainless steel is a duplex spinel oxide, consisting of a magnetite (Fe_3O_4)/nickel ferrite ($NiFe_2O_4$) rich outer layer and an inner layer of iron chromite ($FeCr_2O_4$)/chromia (Cr_2O_3) [54]. The inner chromia/chromite is considered the passivating and protecting layer, key for stainless steel corrosion resistance performance. The oxide outer layer is subjected to dissolution and possible erosion phenomena induced by the water flow. Metal releases in PWRs water cooling circuit is usually modelled on a dissolution/diffusion process through the oxide layers, which affects the metal ionic concentrations of the solution[55]. The formation of a double layered oxide is thought to be due to the immiscibility of different spinels, as within a certain temperature domain, there are stoichiometries that are forbidden [56]. The protective inner oxide formed in stainless steels in PWRs conditions acts as a diffusion barrier, hence, corrosion rate is inversely proportional to the thickness of the oxide which is, in total, considering the magnetite outer layer a few microns thick [57–59]. The literature on low temperature oxidation of 316 L steels at temperature below 100 °C is not as exhaustive as the one on PWRs operating

Table 1
Input for DTT VV cooling circuit simulations for ACPs calculations during UPW operation.

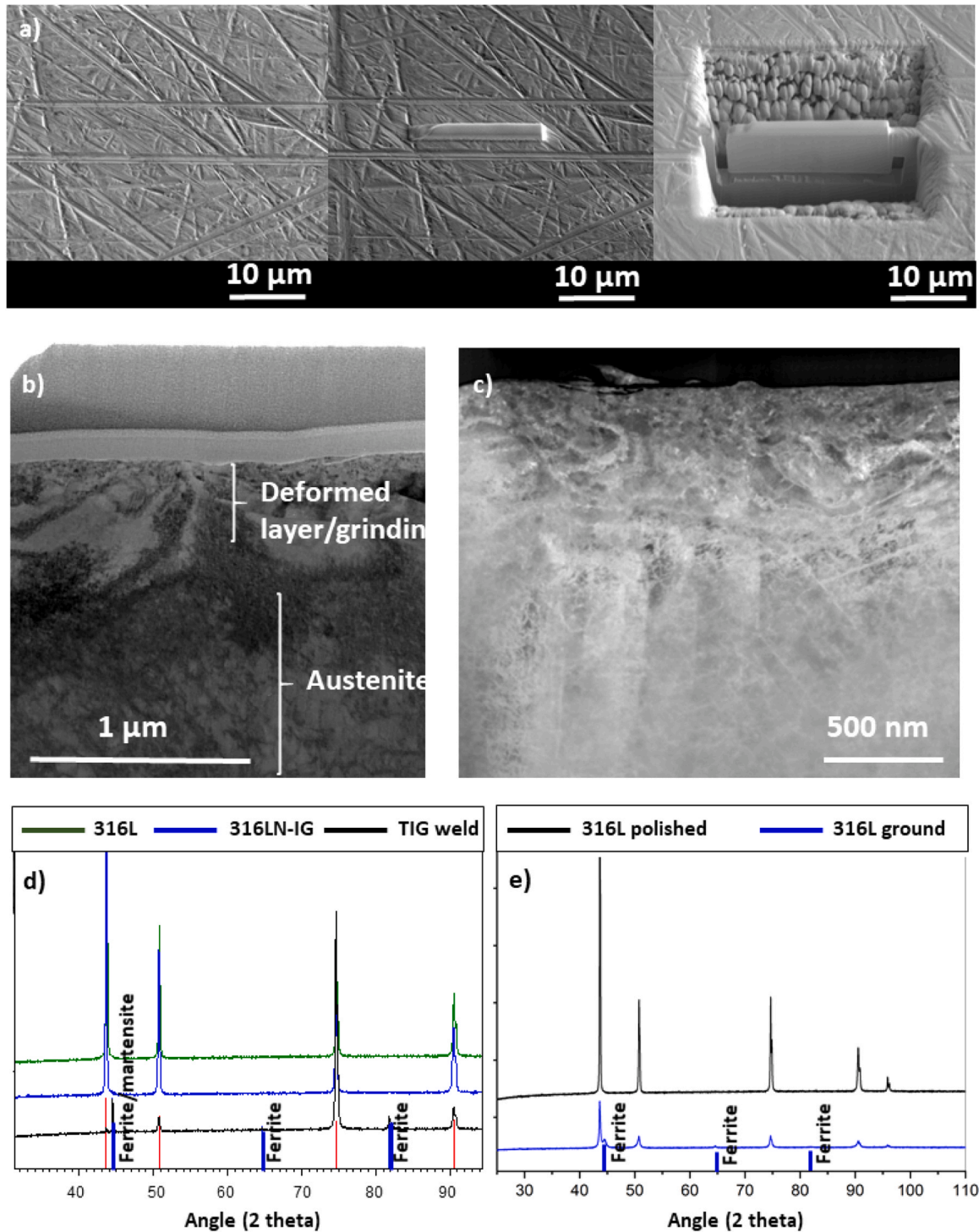| Characteristics of 316 L steel	Roughness (μm)	Initial oxide thickness (nm)	Initial deposit (nm)	Porosity/Tortuosity oxide
	1.3	2.5	20	0.04/1.4
Water chemistry	B (ppm)	Li (ppm)	O_2 (ppm)	H_2 (mL/kg)
	0	0	1	none

Fig. 1. Secondary electron images (SEIs) of samples top surface ground with #1200 SiC grit showing TEM sample preparation; b and c) STEM imaging of sample cross section in a SEM: a superficial deformed layer was visible and was attributed to the grinding procedure; d) XRD analyses on polished samples: austenite peaks were visible on 316 L base metal and 316 LN-IG samples (red lines), additional peaks related to a secondary phase made of ferrite were observed in TIG welds; e) comparison of XRD analyses on 316 L polished sample vs ground sample: ferrite/martensite peaks found on ground samples.

conditions. Previous work considered stainless steel passivated in air [60], or passivated in water solutions at room temperature [52,61]. In this work, stainless steel general corrosion was characterised at 80 °C in water chemistries not previously being investigated.

The sharp decrease of Fe releases in UPW solution accompanied by a decrease of all elements (Cr, Ni, Mn and Mo) after 1 week exposure could be related to the passivation mechanism occurring on stainless steels when a dense and protective oxide layer formed in UPW environment at

80 °C is established, acting as a diffusion barrier and hence limiting further 316 L base metal releases.

Metal releases in samples exposed to 8000 ppm B did not show the same trend of decreasing releases over time. On the contrary, much larger Fe, Cr and Mo releases were measured in the borated water solutions compared to UPW. Gasparrini et al. [30] showed that during 1 week exposure the release of ions from welds and from 316 L base metal in 8000 ppm B environment did not show a significant difference in
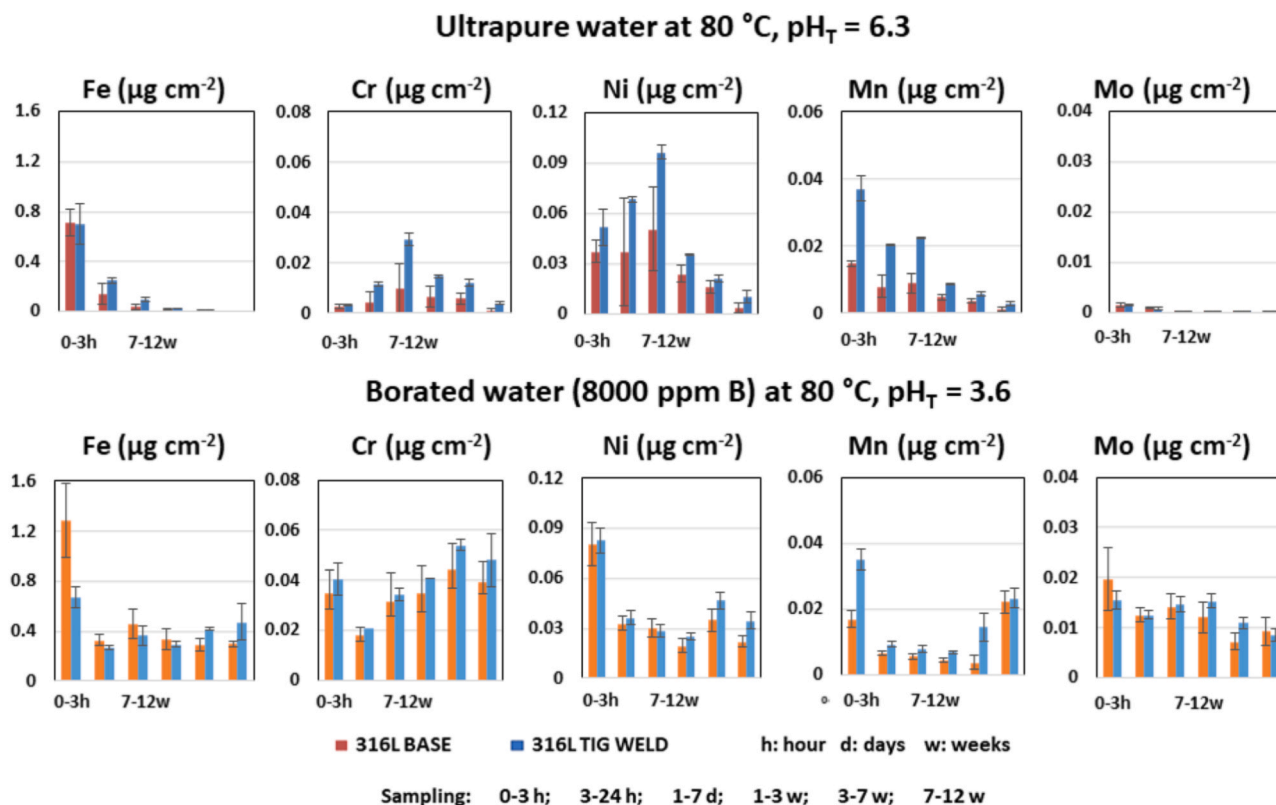
Fig. 2. Released amounts of Fe, Cr, Ni, Mn and Mo per surface area ($\mu g.cm^{-2}$) from 316 L base metal and TIG weld samples exposed to ultrapure water and borated water. Sampling was performed after 3 h, 24 h, 7 days, 3 weeks, 7 weeks and 12 weeks. Error bars represent standard deviation from 6 measurements: three independent specimens were exposed and sampled twice.

terms of Fe, Ni, Cr, and Mo releases compared to the base metal. In both water media, Mn releases from welds were higher than from 316 L base metal as can be seen in Fig. 2, and this could be related to the presence of MnS inclusions in the weld compared to the base metal [30]. Larger releases of Mn from TIG welds compared to 316 L base metal were observed at longer exposure time, up to 12 weeks (see Fig. 2). In Fig. 2, releases did not show a significant difference between base metal and weld during the 12 weeks exposure time for other cations, inferring that microstructure did not influence significantly the release of metal ions into solution, it should be pointed out that the metal release mechanism investigated here came from the martensitic/deformed layer formed on base metals and welds. The oxide layer formed after 12 weeks exposure on 316 L base metals was analysed using STEM analyses, chemical characterisation was conducted with EDX and EELS (see Fig. 3).

The oxide layer formed after 12 weeks exposure at 80 °C was approximately 20 nm thick. The oxide layer was formed on top of the martensitic deformed layer, see Fig. 3. EELS analyses showed the presence of an oxide in both UPW and 8000 ppm B samples, and differences in thickness or chemical composition were not clearly obvious from STEM-EELS data (see Fig. 3a). STEM-EDX and EELS clearly showed the presence of a chromium rich oxide layer, see image in Fig. 3, but the chemical resolution in this geometric configuration could not reveal the chemistry profile across the <20 nm oxide layer, mostly due to the intrinsic roughness of the interface. APT was used as alternative technique to assess the chemical composition at the atomic scale of the oxide layer and understand if any potential difference between the passivating oxide layer formed in UPW compared to 8000 ppm B existed. APT samples were made from specimens extracted from the samples previously analysed by TEM (shown in Fig. 3). APT 3D reconstructions are shown in Fig. 4 and chemical analyses reconstruction across the passive oxide layer found in the two aqueous environments are shown in Fig. 5. Independent set of samples were prepared and analysed and in Fig. 5

only two representative results are shown.

APT revealed the chemical analysis composition across the <20 nm thick oxide layer on both UPW and 8000 ppm B samples. APT analysis showed the presence of a Ni-enriched sub-oxide layer in both UPW samples and 8000 ppm B samples, within this sub-oxide layer at the metal/oxide interface some samples also revealed an enrichment in Cu. Above this sub-oxide layer a transition layer was observed and it was characterised by a decrease of Fe and Ni, while Cr – O increase.

The sub-oxide layer is also known in the literature as denuded zone or depleted zone and it is a region characterised by a depletion of all elements that were going to oxidise. Ni enrichment observed here in the oxide analysed on samples exposed to 8000 ppm B could be related to that previously observed ahead of the chromia/oxide scale in SCC tips [62], but no information, to the best of author's knowledge, was ever reported on passive oxide surface layers. The chemical composition of the oxide layer was different in UPW samples compared to 8000 ppm B samples, while the thickness varied but remained in the same range (<20 nm) for both conditions. UPW oxide layer was characterised by a flat profile of fixed concentration of Cr and O (40: 45) that acts as a protective diffusion barrier given the very low metal releases quantified by ICP-MS and shown in Fig. 2. The oxide formed in 8000 ppm B environment instead, did not show a fixed chemical composition and the enriched composition of Ni and Mo in the oxide layer are in line with the higher releases measured in the 8000 ppm B water proving that mass transfer of these elements occur and therefore the oxide is not protective. The mass transfer is definitely affected by water chemistry characteristics, in particular concentration of the reactants and pH_T. pH_T notably controls the amount of H^+, or H_3O^+, in the water which affects corrosion rates: a low pH, like in the case of 8000 ppm B added as H_3BO_3 in water at 80 °C, results in higher concentration of H^+, or H_3O^+.

Metal releases measured by ICP-MS quantified from samples submerged in either UPW or 8000 ppm B were indeed substantially
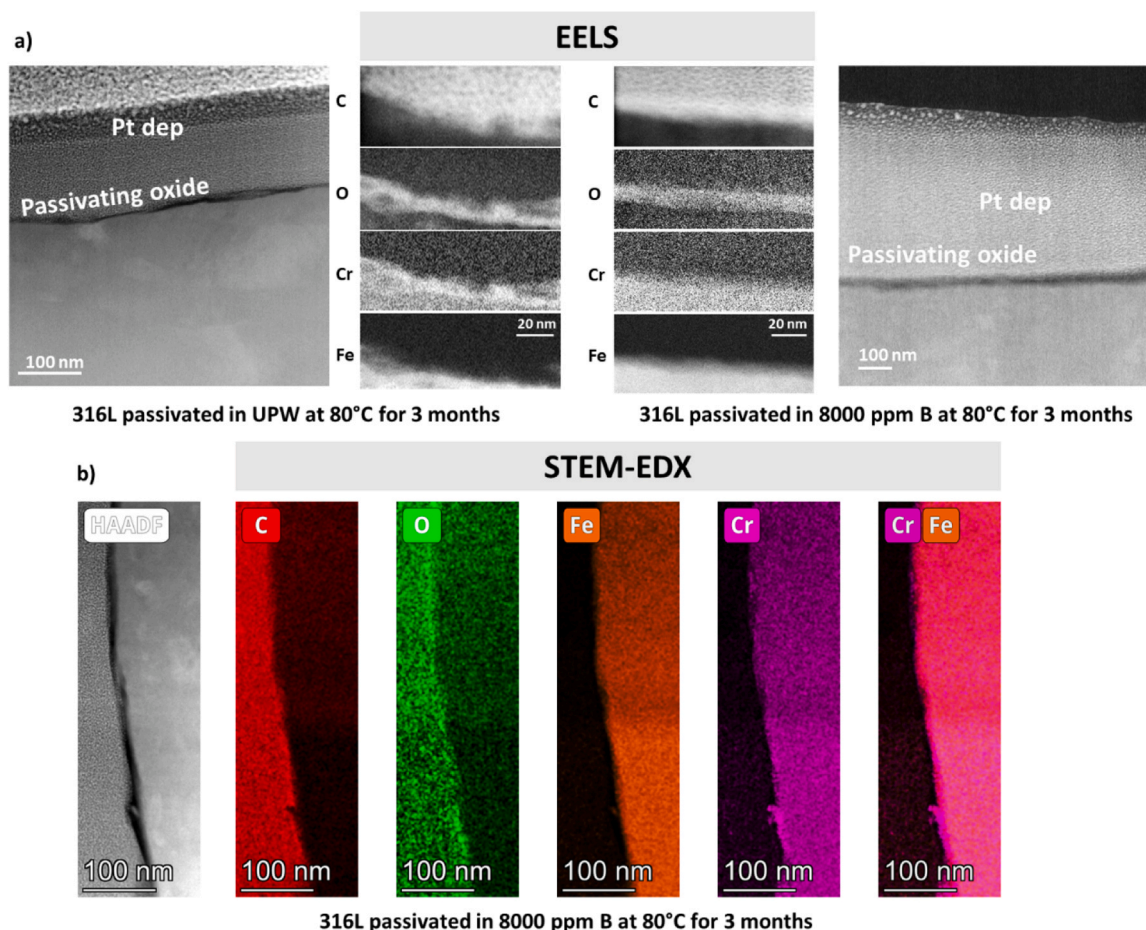
Fig. 3. STEM images on samples extracted from 12 weeks passivated 316 L base samples exposed to UPW and 8000 ppm B at 80 °C; a) EELS elemental maps showing the chemical composition of the oxide layer in UPW and 8000 ppm B passivated samples; b) EDX elemental maps showing chemical composition of the oxide on 8000 ppm B passivated samples. Carbon is linked to the protective e-Pt layer.
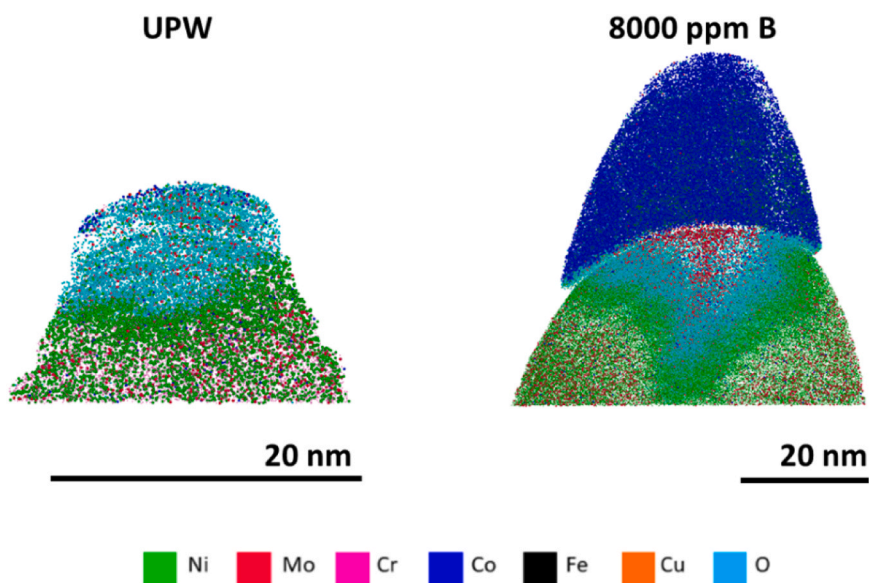

Fig. 4. APT reconstruction for two tips representatives of the set of samples analysed for the 2 aqueous environments, in blue is shown the protective Co cap deposited on top of samples prior to APT samples preparation (Co cap was less thick in the UPW sample APT tip, but it is still possible to delineate the oxide top surface).
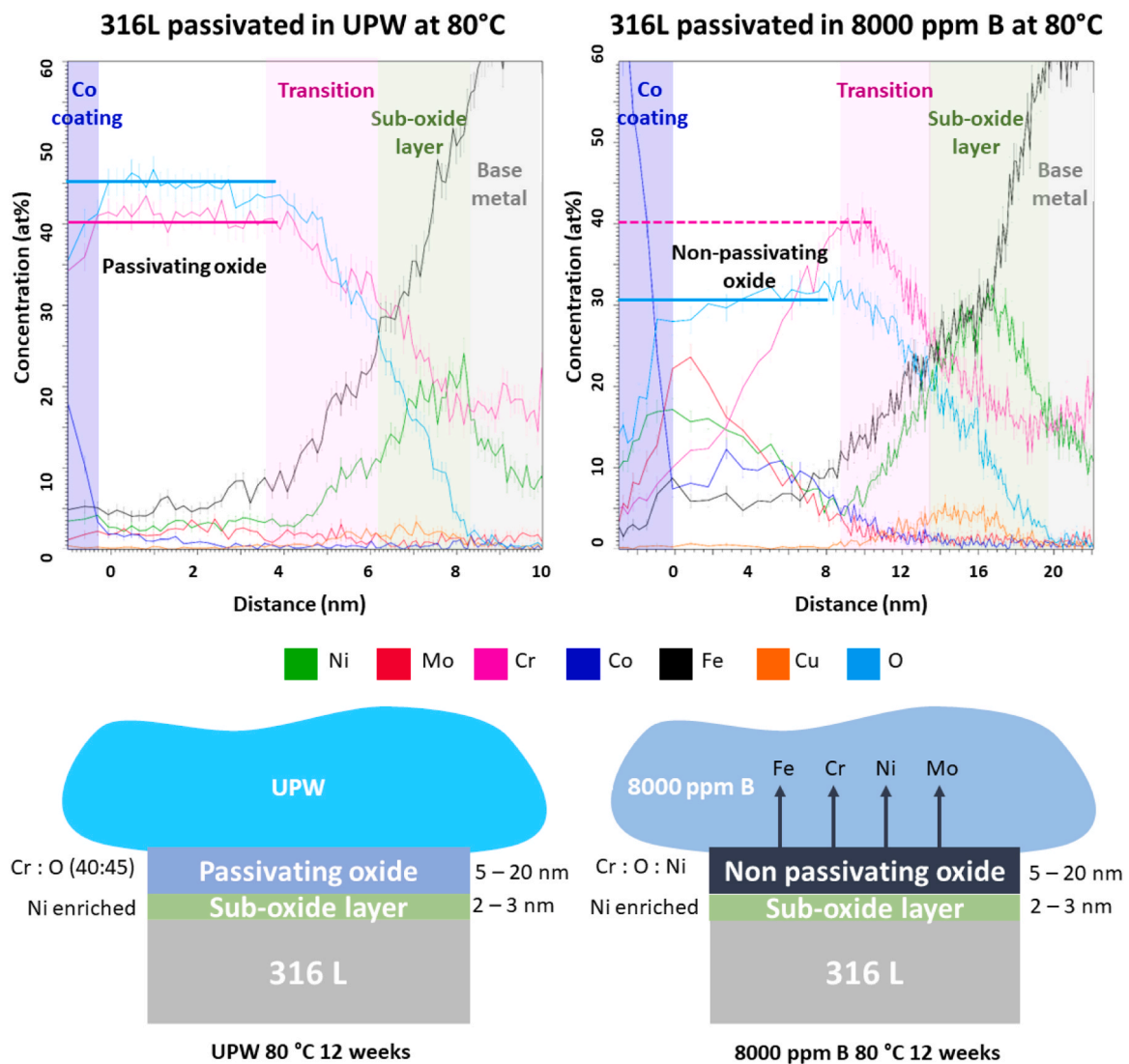
Fig. 5. Top: APT data showing chemical analyses profiles across the oxide layer formed on 316 L steels samples passivated in ultrapure water and borated water (same samples used in experiments shown in Fig. 2 and previously analysed by TEM) for 12 weeks at 80 °C. Samples were coated by 200 nm Co prior extraction by FIB of APT tips to protect the oxide layer. APT data showed a different distribution of chemical elements and the presence of base metal - enriched sub-oxide layer - a transition and an outer oxide layer. The passivating oxide layer formed in UPW environment was formed by a protective Cr – O oxide characterised by constant composition highlighting its protectiveness, the outer oxide formed on 8000 ppm B water after 12 weeks exposure was characterised by Cr – O – Ni. Bottom: Schematic showing the structure of the oxide layer formed: a Ni-enriched sub-oxide layer was observed in both UPW and 8000 ppm B passivated samples. The oxide layer was different between UPW and 8000 ppm B oxides: a chromite oxide (Cr:O 40:45) was found on UPW samples while 8000 ppm B showed a non passivating structure since a gradient characterises Cr profile, Ni and Mo are selectively being released in the water and are shown to be enriched in the outer oxide.

different as shown in Fig. 2. By plotting the metal releases over time from the experiments shown in Fig. 2 as a ratio between the releases in 8000 ppm B compared to UPW it was possible to note that releases for all elements were higher when exposed to 8000 ppm B, see Fig. 6. Mo showed the highest change in release when in contact with 8000 ppm B (up to 100 times larger) and the increase of Mo in the non passivating oxide layer can be observed in Fig. 5 on 8000 ppm B samples. Fe releases were 100 times larger at 12 weeks exposure while Cr releases were 30 times larger at 12 weeks exposure in 8000 ppm B environment, see Fig. 6. Larger releases of Cr and Fe infer that the oxide layer formed on 316 L in 8000 ppm B was not protective and did not act as a diffusion barrier, as also shown by chemical analyses in Fig. 5. The 3 nm chromite layer analysed on UPW samples, instead, acted as a passivating layer.

Results from metal release experiments showed an enhanced release for all cations from stainless steel exposed to 8000 ppm B compared to UPW. The metal release rates measured with these experiments served not only to assess the general metal release rates from stainless steels at temperature and water chemistries relevant to DTT VV cooling circuit, they also served as input data for ACPs calculations using the code developed by CEA called OSCAR-Fusion v1.3[34]. Using OSCAR-Fusion v1.3 as simulation tool it was not possible to tailor the water chemistry to the regime needed for DTT VV, 8000 ppm B (upper limit set to <100 ppm B), so it was necessary to input release rates measured from experiments to simulate realistically the formation and redeposition of ACPs in the DTT VV circuit. UPW water chemistry properties and temperature conditions relevant to DTT VV cooling circuit, instead, could be simulated. Release rates measured through the experiments in this work were plotted together with release rates obtained from simulations for UPW (see Fig. 7). The trend, for both experiments and models, showed an initial decreasing slope. Release rates obtained from OSCAR-Fusion v1.3 reached a constant value after approximately 500 hours, while in experiments they all showed a continued decreasing trend. In all experiments, steady state was not reached after 12 weeks exposure. Release rates between experiments and simulations were closer at long
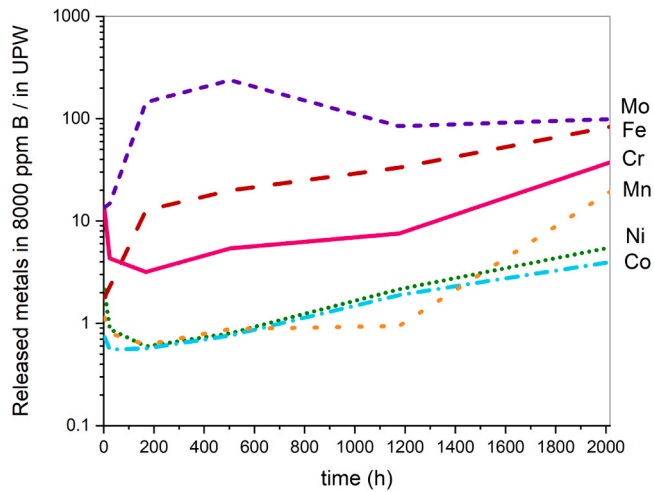
Fig. 6. Ratio of metal releases rates (measured by ICP-MS of Fe, Ni, Cr, Mo, Mn and Co) in borated water vs ultrapure water with exposure time.

exposure times.

Release rates measured on samples exposed to 8000 ppm B were roughly 100 times larger for Fe and 30 times larger for Cr at long exposure times. This value was used as input into the DTT VV model written in OSCAR-Fusion v1.3 to compare the amount of ACPs formed

and deposited in components outside the bio shield when boric acid is injected in the DTT VV cooling circuit during high performance phases compared to operation in pure UPW. However, this is an approximation on CPs formation/redeposition since the water chemistry (water pH) could not be modelled with OSCAR-Fusion v1.3 for 8000 ppm B water chemistries. The addition of boric acid is required when it is necessary to shield the superconducting magnets from neutrons. Given the release law in the simulation code is defined for reducing conditions only, to perform calculations on ACPs in the DTT VV the release rates measured experimentally (Fig. 7) were used: Fe releases at longest exposure times were taken as representative release rates. Corrosion rates were set to be 10 times larger than the release rates as reported in Molander et al.[13] (approximation valid for water cooling circuit with low water velocity, 2 m/s). The release rates for UPW cooling circuit were set in OSCAR-Fusion v1.3 to be: 1.2e-11 g s^{-1}m^{-2}, while for 8000 ppm B were 10e-10 g s^{-1}m^{-2}.

Fig. 8a shows the schematic of the DTT VV cooling circuit modelled for the prediction of ACPs formation during a neutronic phase representative of DTT. Fig. 8b shows the CAD design of the DTT VV structure (top right) which is situated inside the tokamak reactor hall. The data plotted showed the surface activity of a component (e.g. pipe situated in the auxiliary building outside the bioshield) induced by ACPs products formation in the VV under neutronic bombardment and redeposition outside the bioshield. Dashed lines represent the ACPs formation and redeposition using 8000 ppm B, continuous lines represent ACPs using UPW. The main source of activity from ACPs deposits to personnel are
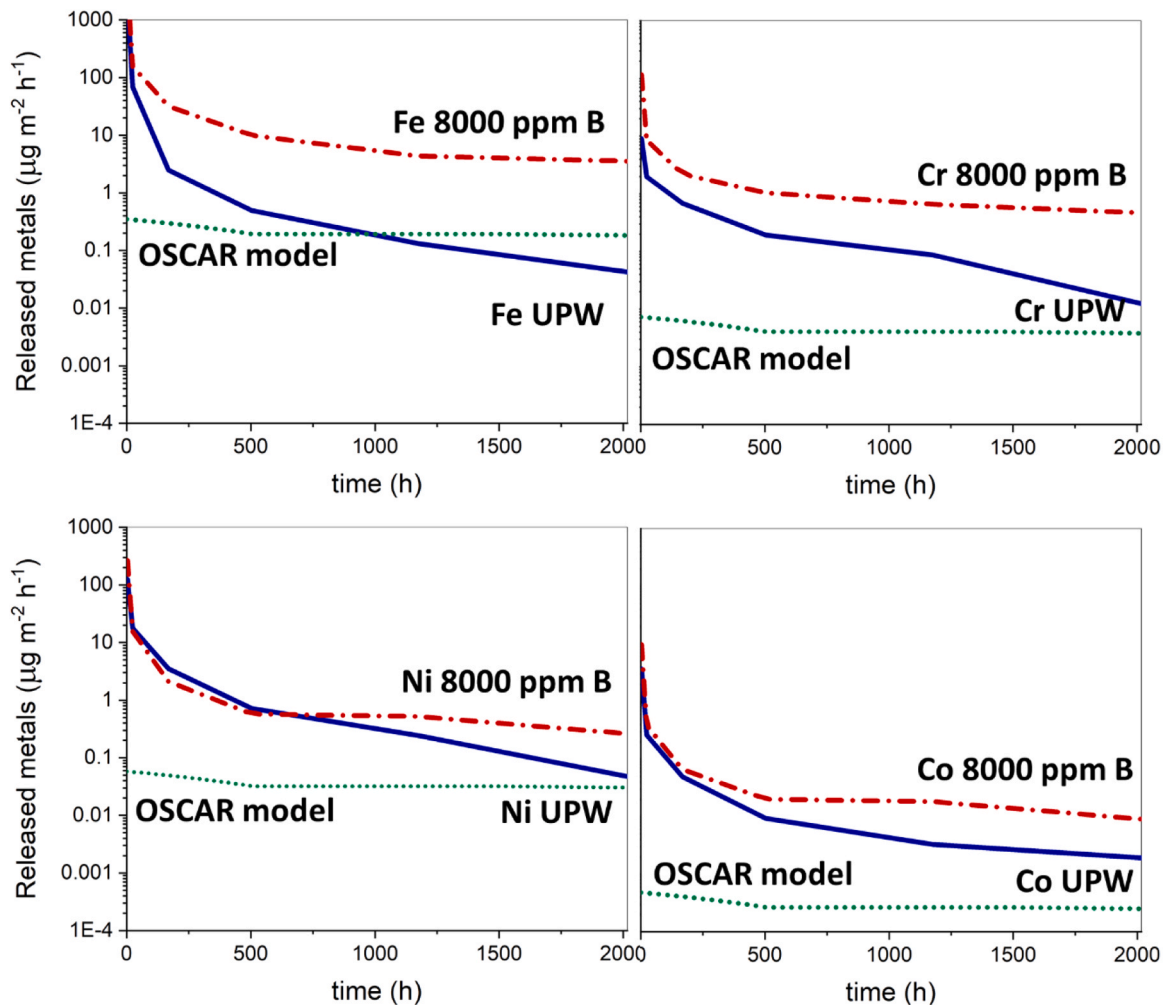

Fig. 7. Trend of metal release rates from experiments (this work) and comparison with release rates stored in OSCAR-Fusion v1.3: an ACPs code developed for fission reactor and tailored to fusion reactors for same water temperature and water chemistry (only UPW could be modelled with OSCAR-Fusion v1.3).
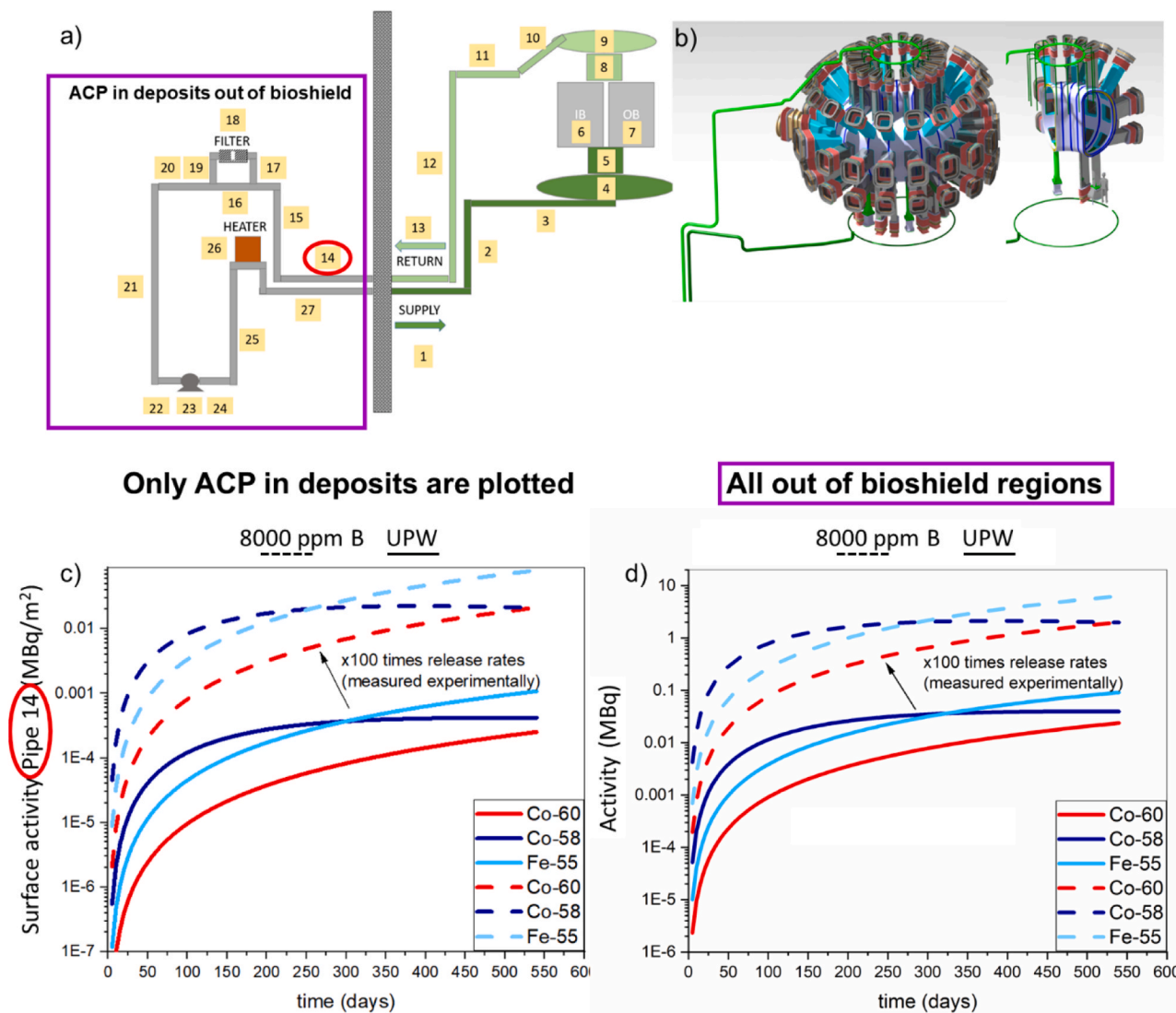
Fig. 8. a) Schematic of the DTT VV cooling circuit loop modelled with OSCAR-Fusion v1.3 used to estimate ACPs formation and redeposition during DTT operation. b) CAD design of the DTT VV structure within the tokamak hall; c) ACPs deposited in components and piping outside the bioshield on a single pipe c) or in the entire circuit outside the bioshield d). ACPs results are related to a 18 months neutronic scenario, related to the production of 7.87×10^{19} n as described in Villari et al. [18] considering an ideal continous operation (no alternation between wetting/baking stages).Dashed lines represent the ACPs formation and redeposition using 8000 ppm B, continuous lines represent ACPs using UPW.

related to Co-60 and Co-58 due to their gamma emission. The total activity of deposits accumulated in all components and piping outside the bioshield was plotted in Fig. 8d. Even though the activity levels are very limited (and should not be used for radioprotection purposes), higher metal release rates due to the addition of boric acid led to a higher total ACPs deposit out of bioshield. The total activity in the loop outside the bioshield when boric acid was used was roughly 100 times larger than when UPW was used, in line with the 100 times larger releases measured experimentally (see Fe releases at long exposure in Fig. 7a). Higher ACPs redeposition was induced by higher general release rates induced by the presence of boric acid as a coolant media, this simulation is not, however, taking into consideration water pH effect. A newer version of OSCAR-Fusion without limitations on boric acid addition should be implemented to simulate the realistic condition of using 8000 ppm B after validation with experiments. It should be noted that higher corrosion products and larger ACPs redeposition, when boric acid is used in the primary cooling circuit, were observed during operation of the PWRs fleet [63].

After considering general corrosion of stainless steel, another

important aspect was investigated to assess the reliable operation of a nuclear fusion reactor: SCC initiation. Chloride salts are the benchmark when it comes to establish SCC susceptibility. NaCl was used to assess SCC susceptibility of the two water chemistries induced passive layers to discern potential drawbacks of using borated water instead of UPW. Furthermore, Cl SCC cracking have occurred in many systems where it was not foreseen. One of the latest cases in the fusion world preventing the on time assembly of one of the most important magnetic confined nuclear fusion experiment is indeed a chloride stress corrosion cracking failure [29]. Stainless steels are prone to SCC when exposed to acidic water chemistries, but highly concentrated borated water in low temperature regimes are not well studied. SCC initiation testing was performed on 316 L samples passivated at 80 °C for 12 weeks (the same samples tested in Figs. 2–5). The method was previously tested in Yazdanpanah et al. [37]. Specimens passivated in UPW for 12 weeks (labelled as UPW90 in Fig. 9) behaved better than specimens passivated in boric acid for 12 weeks (labelled as CBA90 in Fig. 9) when tested without strain condition. The potentiodynamic polarization measurements were performed increasing the potential gradually, so it was not
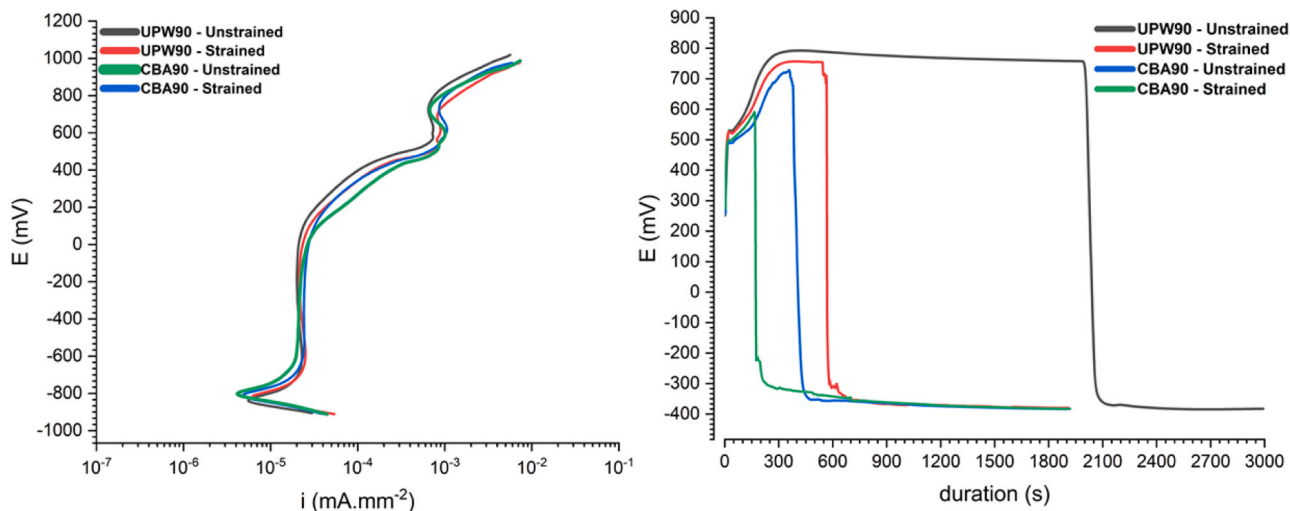
Fig. 9. Potentiodynamic (left) and galvanostatic (right) results of sample passivated after 12 weeks in UPW (UPW90) or 8000 ppm B (CBA90).

possible to test the robustness of the passive oxide layer. The degree of protection offered by the passive layer protectiveness for samples passivated in either UPW or 8000 ppm B were tested with galvanostatic experiments under constant current density. Galvanostatic polarization results confirmed substantially better performance of the passive layer in unstrained condition of samples passivated in UPW compared to borated water. By applying a stress level 10% greater than the yield stress, the resistance of the passive layer decreased dramatically for samples passivated in both conditions, with the worst performance of the samples passivated in borated water. Furthermore, the maximum recorded potential in both unstrained and strained states revealed higher potentials for UPW compared to borated water, indicating higher resistance of the passive layer. However, such a decrease in electrochemical polarization characteristics after tensile straining of the samples was also observed in authors' previous investigations[37].

Further SEM microstructural analysis of the electrochemically polarized surface (after galvanostatic measurements) of the specimens, as shown in Fig. 10, highlights the presence of SCC initiation sites along the grain boundaries from existing pits for both cases, revealing substantially deeper pits and higher density of cracks for the case of specimens passivated in borated water solution. Such an observation could be attributed to lower resistance of the passive layer to localized corrosion attack, which could directly lead to a shorter time for the localized corrosion attack and SCC formation to proceed. SCC initiation analysis showed that the occurrence of SCC in this environment and

experimental condition is inevitable as reported extensively during the past decades, the question is how severe is the condition before the cracks reach a critical size. As a result, higher susceptibility to cracking during the early stages of crack initiation could substantially lead to higher density and size of the cracks during the propagation stage. It could be stated that the passivation in borated water leads to lower resistance of the native oxide layer to localized corrosion attack, leading to higher SCC susceptibility of the borated water specimens.

UPW passivated surfaces showed a larger presence of small pores spread over the surface compared to 8000 ppm B passivated surfaces, see Fig. 10. In 8000 ppm B passivated surfaces the corrosion attack is localized on specific sites. As a result, local features are readily available for passing higher current density (smaller surface area) leading to a higher localized corrosion rate. Higher corrosion rates consequently lead to the formation of deeper pits.

4. Conclusions

General corrosion of 316 L base metals and TIG welds in nuclear fusion experimental reactors water chemistries was studied experimentally exposing samples to UPW and 8000 ppm B solutions for 12 weeks at 80 °C. The two solutions are needed to operate the DTT VV cooling circuits: UPW during the non-nuclear phase of operation of the reactor while 8000 ppm B (95% enriched in ^{10}B) is needed during high performance tests. In this work general corrosion and SCC initiation was
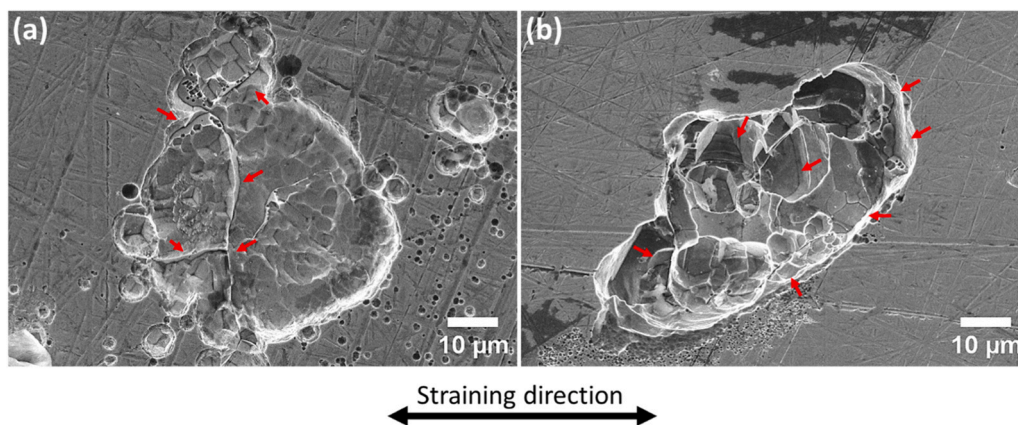

Fig. 10. SE images of electrochemically polarized surface after galvanostatic measurements: a) samples previously passivated in UPW; b) samples previously passivated in borated water for 12 weeks; red arrows highlight microcracks.

studied for the two water chemistries, it should be noted that the fore-seen operating condition consider the possible alternation between UPW, borated water and an additional stage called baking using hot nitrogen gas.

General corrosion was measured using metal release experiments: for all cations studied here, Fe – Cr – Ni – Mn – Mo and Co, releases were much higher in 8000 ppm B solutions compared to UPW. After 12 weeks, Fe and Mo releases were approximately 100 times higher in 8000 ppm B than UPW. Cr releases were approximately 30 times larger in 8000 ppm B.

Characterisation with STEM-EDX revealed the oxide in both water chemistries to be approximately 20 nm thick. EELS characterisation showed the oxide layer to be Cr rich in both environments.

APT characterisation of the oxide layers revealed the oxide to be comprised of Ni-enriched sub-oxide layer in both UPW samples and 8000 ppm B samples. Above this sub-oxide layer a transition into an oxide layer was observed. The oxide layer formed on UPW samples was characterised by a flat and constant chromite layer (Cr: O - 40: 45) that acted as a protective barrier in line with the very low metal releases quantified by ICP-MS (metal release experiments). The oxide formed in 8000 ppm was characterised by a non-homogeneous chemical composition: Cr was not constant, Ni and Mo were enriched at the interface oxide/water solution: this is consistent with the higher releases measured in the 8000 ppm B water inferring that metal transfer develops through the non-protective oxide layer.

Release rates measured experimentally were used to estimate the formation of ACPs outside the bioshield of the DTT. It was observed that when 8000 ppm B was used, higher ACPs deposits were formed and redeposited on components and piping outside the bioshield.

The addition of boric acid was not only detrimental for general corrosion and ACPs redeposition, the acidic environment induced by the presence of boric acid also influenced SCC. SCC initiation tests were performed using microcapillary test, the oxide layer formed in 8000 ppm B was less protective and more prone to SCC initiation in both unstrained and uniaxially tensile strained conditions compared to the protective oxide layer formed in UPW.

Overall this work highlights the need to improve water chemistry and cooling circuit definition in nuclear fusion experimental reactors operating with 8000 ppm B to avoid SCC issues and minimisation of ACPs formation and redeposition.

Author statement

C.G. performed the literature survey, planned experiments and simulations, conducted metal release experiments and characterisation of bulk samples with TEM, SEM and XRD, performed ACPs simulations, coordinated the project, wrote the manuscript, acquired funding; J.O.D. planned and performed APT experiments and analyses, performed FIB-SEM preparation of APT samples, wrote and reviewed the manuscript, supported with facilities access at Imperial College London; A.Y. planned and performed SCC initiation testing and characterisation of samples afterwards with SEM, wrote and reviewed the manuscript; R.S. analysed APT data and created APT images; G.D. performed STEM-EDS and EELS experiments, reviewed and edited the manuscript, supported with facilities access at IIT Genova; M.D. supported with facilities access in Padua University enabling A.Y. experiments and work, G.G.S. supported with literature review and technical details, reviewed and edited the manuscript. S.P. supported APT experiments, reviewed and edited the manuscript, supported with funding acquisition and facilities access at Imperial College London; M.R.W., reviewed and edited the manuscript, supported with funding acquisition and facilities access at Imperial College London; D.B. performed ICP-MS analyses and aid their experimental procedure optimisation, P.P. supported ICP-MS facilities access, N.T. supported access to OSCAR-Fusion v1.3, supported ACPs simulations and facilities access in ENEA Frascati; G.M. input neutron reaction rates to calculate ACPs with OSCAR-Fusion v1.3 and aid

plotting ACPs; F.D. supported access and use of OSCAR-Fusion v1.3, reviewed and edited the manuscript, M.D.P. supported facilities putting up in Consorzio RFX, R.V. supported C.G. with funding acquisition and neutronics calculations, enabled access to ACPs software and supported access to ENEA Frascati facilities, P.S. supported C.G. obtaining funding and enabled granting access to all facilities.

Declaration of Competing Interest

The authors declare that they have no known competing financial interests or personal relationships that could have appeared to influence the work reported in this paper.

Data Availability

Data will be made available on request.

Appendix

Atom probe tomography [64] samples were fabricated using Focused Ion Beam site specific liftout [65] on silicon microposts (Cameca), with a 200 nm layer of magnetron sputter coated cobalt capping layer prior to FIB lifting preparation in order to preserve and delineate the surface during atom probe analysis. Cobalt was selected as it is clearly visible during FIB sample preparation, not present within the alloy or electrochemical experimental setup and evaporates at a similar field to the alloy during APT analysis [66]. A Thermofisher Scientific Helios 5 Ga+ FIB was used to fabricate the samples, with 30 kV Ga+ ions used for liftout and sharpening and 2 kV Ga+ used to remove damaged surfaces, leaving a small layer of undamaged Co above the oxide. APT analysis was carried out in a LEAP 5000XR atom probe (Cameca) at a base temperature of 60 K, a base pressure of $4E^{-11}$ Torr, laser pulse energy of 30 pJ, a laser pulse frequency of 100 kHz and a data collection rate of 0.005 ions per pulse. APT data analysis was carried out with AP Suite 6.1 software using a voltage based reconstruction protocol with a k-factor of 3.3 and an ICF of 1.65. Two samples of each material were successfully analysed with a visible Co capping layer still present within the reconstructed volume.

Decomposed iso-concentration surfaces of oxygen were used to isolate the complex interface between metal capping layer and the oxide layer and cylindrical Regions of Interest were used to generate 1D concentration profiles tangential to the oxygen surface. Concentration profiles using a 500 ions per step/sample approach were plotted using the summation of all ions, with complex ions decomposed where present.

References

[1] International Atomic Energy Agency, Nuclear energy for a net zero world, 2021.

[2] S. Dickman, Nations meet to plan for world nuclear fusion effort, Nature, 329, 6142, pp. 753–753, 1987.

[3] M. Barbarino, On the brink of a new era in nuclear fusion R&D, Nat. Rev. Phys., 4, 1, 2–4, 2022.

[4] G. Federici, L. Boccaccini, F. Cismondi, M. Gasparotto, Y. Poitevin, I. Ricapito, An overview of the EU breeding blanket design strategy as an integral part of the DEMO design effort, Fusion Eng. Des. 141 (December 2018) (2019) 30–42.

[5] G. Mazzitelli, et al., Role of Italian DTT in the power exhaust implementation strategy, Fusion Eng. Des. 122 (October 2018) (2019) 1–5.

[6] T. Donné and W. Morris, European research roadmap to the realisation of fusion energy, 2018.

[7] A.J.H. Donné, The European roadmap towards fusion electricity, Philos. Trans. R. Soc. A Math. Phys. Eng. Sci. 377 (2141) (2019).

[8] R. Ambrosino, DTT - Divertor Tokamak Test facility: a testbed for DEMO, Fusion Eng. Des. 167 (January) (2021) 112330.

[9] R. Albanese, et al., Design review for the Italian Divertor Tokamak Test facility, Fusion Eng. Des. 146 (October 2018) (2018) 194–197.

[10] R. Martone, R. Albanese, F. Crisanti, A. Pizzuto, and P. Martin, DTT Divertor Tokamak Test Facility Interim Design Report, "Green Book" ⟨https://www.dtt-dms.enea.it/share/s/avvglhVQT2aSkSgV9vuEtw⟩, 2019.

[11] P. Barabaschi, Y. Kamada, H. Shirai, J. Integrated, and P. Team, Progress of the JT-60SA project, 2019.

[12] G. Lee, et al., The KSTAR project: an advanced steady state superconducting tokamak experiment, Nucl. Fusion 40 (3Y) (2000) 575–582.

[13] A. Molander, Corrosion and water chemistry aspects concerning the tokamak cooling water systems of ITER, STUDSVIK/N. -06/186 TW5-TVM-LIP (2006).

[14] P. Lorenzetto, M. Hélie, A. Molander, Stress corrosion cracking of AISI 316LN stainless steel in ITER primary water conditions, J. Nucl. Mater. 233–237 (2) (1996) 1387–1392.

[15] S. Wikman, J. Eskhult, and A. Molander, Experimental assessment of materials exposed to coolant water under ITER relevant operational conditions.

[16] C. Gasparrini, et al., Water degradation in ITER neutral beam test facility cooling circuits, IEEE Trans. Plasma Sci. (2022) 1–5.

[17] C. Cavallini, et al., Investigation of corrosion-erosion phenomena in the primary cooling system of SPIDER, Fusion Eng. Des. 166 (January) (2021) 112271.

[18] R. Villari, et al., Nuclear design of Divertor Tokamak Test (DTT) facility, Fusion Eng. Des. 155 (September 2019) (2020).

[19] EPRI, Pressurized water reactor primary water chemistry guidelines, 1, 2014.

[20] EPRI, An evaluation of Enriched Boric Acid in European PWRs, 1003124, p. 114, 2001.

[21] J.H. Park, O.K. Chopra, K. Natesan, and W.J. Shack, Boric acid corrosion of light water reactor pressure vessel materials, NUREG/CR-6875 ANL-04/08, 2005.

[22] E. Lo Piccolo, R. Torella, N. Terranova, L. Di Pace, C. Gasparrini, M. Dalla Palma, Preliminary assessment of cooling water chemistry for fusion power plants, Corros. Mater. Degrad. 2 (3) (2021) 512–530.

[23] M.P. Ryan, D.E. Williams, R.J. Chater, B.M. Hutton, D.S. McPhail, Why stainless steel corrodes, Nature 415 (6873) (2002) 770–774.

[24] EPRI, Materials reliability program: boric acid corrosion guidebook, Revision 2: Managing boric acid corrosion issues at PWR power stations (MRP-058, Rev 2), 2012.

[25] F. Cattant, Materials Ageing In Light-water Reactors, Springer International Publishing, Cham, 2022.

[26] R.O. Müller, Crevice corrosion test for stainless steels in chloride solutions. Passivity of Metals and Semiconductors, Elsevier, 1983, pp. 347–352.

[27] Z. Shen, D. Du, L. Zhang, S. Lozano-Perez, An insight into PWR primary water SCC mechanisms by comparing surface and crack oxidation, Corros. Sci. 148 (December 2018) (2019) 213–227.

[28] Counting the cost of cracking, Nucl. Eng. Int., no. August 2022, 2022.

[29] World Nuclear News, Defects found in two key components of ITER's tokamak, 2022.

[30] C. Gasparrini, et al., Water chemistry in fusion cooling systems: borated water for DTT vacuum vessel, IEEE Trans. Plasma Sci. (2022) 1–5.

[31] E. Martelli, et al., Design status of the vacuum vessel of DTT facility, Fusion Eng. Des. 172 (July) (2021) 112760.

[32] F. Dacquait, et al., Simulations of corrosion product transfer with the OSCAR V1.2 code, Nucl. Plant Chem. Conf. Pap. Ref. (n 193 P1-24) (2012).

[33] F. Dacquait et al., The OSCAR code: a simulation tool to assess the PWR contamination for decommissioning, DEM 2021 – Int. Conf. Decommissioning Challenges, Sep 2021, Avignon, Fr. pp.Oral T04 / 054. cea-03434535, 2021.

[34] F. Dacquait, J.B. Genin, L. Brissonneau, Modelling of the contamination transfer in nuclear reactors: the OSCAR code applications to SFR and ITER, 1st IAEA Work. Chall. Cool. Fast Neutron Spectr. Syst. (July) (2017) 5–7.

[35] Z. Shen, et al., Microstructure understanding of high Cr-Ni austenitic steel corrosion in high-temperature steam, Acta Mater. 226 (2022) 117634.

[36] P. Dong, G.G. Scatigno, M.R. Wenman, Effect of salt composition and microstructure on stress corrosion cracking of 316L austenitic stainless steel for dry storage canisters, J. Nucl. Mater. 545 (2021) 152572.

[37] A. Yazdanpanah, M. Franceschi, R.I. Revilla, S. Khademzadeh, I. De Graeve, M. Dabalà, Revealing the stress corrosion cracking initiation mechanism of alloy 718 prepared by laser powder bed fusion assessed by microcapillary method, Corros. Sci. 208 (September) (2022) 110642.

[38] P.L. Andresen, Understanding and predicting stress corrosion cracking (SCC) in hot water. Stress Corrosion Cracking of Nickel Based Alloys in Water-cooled Reactors, Elsevier,, 2016, pp. 169–238.

[39] D.D. Macdonald, The electrochemical nature of stress corrosion cracking. Stress Corrosion Cracking of Nickel Based Alloys in Water-cooled Reactors, Elsevier, 2016, pp. 239–294.

[40] R.W. Staehle, Historical views on stress corrosion cracking of nickel-based alloys. Stress Corrosion Cracking of Nickel Based Alloys in Water-cooled Reactors, Elsevier,, 2016, pp. 3–131.

[41] A. Yazdanpanah, L. Pezzato, M. Dabalà, Stress corrosion cracking of AISI 304 under chromium variation within the standard limits: Failure analysis implementing microcapillary method, Eng. Fail. Anal. 142 (September) (2022).

[42] A. Yazdanpanah, et al., Unveiling the impact of laser power variations on microstructure, corrosion, and stress-assisted surface crack initiation in laser powder bed fusion-processed Ni-Fe-Cr alloy 718, Electrochim. Acta 476 (November 2023) (2024) 143723.

[43] S. Torchio, Stress corrosion cracking of type aisi 304 stainless steel at room temperature; influence of chloride content and acidity, Corros. Sci. 20 (4) (1980) 555–561.

[44] X. Guo, Y. Wang, T. Yao, C. Mohanty, J. Lian, G.S. Frankel, Corrosion interactions between stainless steel and lead vanado-iodoapatite nuclear waste form part I, NPJ Mater. Degrad. 4 (1) (2020) 13.

[45] M. Atapour, X. Wang, K. Färnlund, I. Odnevall Wallinder, Y. Hedberg, Corrosion and metal release investigations of selective laser melted 316L stainless steel in a synthetic physiological fluid containing proteins and in diluted hydrochloric acid, Electrochim. Acta 354 (2020) 136748.

[46] M. Atapour, Z. Wei, H. Chaudhary, C. Lendel, I. Odnevall Wallinder, Y. Hedberg, Metal release from stainless steel 316L in whey protein - and simulated milk solutions under static and stirring conditions, Food Control 101 (February) (2019) 163–172.

[47] ASTM D4453-17, Standard practice for handling of high purity water samples, 2017.

[48] ASTM C1220-17, Standard test method for static leaching of monolithic waste forms for disposal of radioactive waste, 2017.

[49] A.C. Bevilacqua, Ultrapure water–the Standard for resistivity measurements of ultrapure water, Semicond. Pure Water Chem. Conf. (1998) (1998) 2–5.

[50] M. Carter, et al., On the influence of microstructure on the neutron irradiation response of HIPed SA508 steel for nuclear applications, J. Nucl. Mater. 559 (2022) 153435.

[51] A. Aitkaliyeva, J.W. Madden, B.D. Miller, J.I. Cole, J. Gan, Comparison of preparation techniques for nuclear materials for transmission electron microscopy (TEM), J. Nucl. Mater. 459 (2015) 241–246.

[52] M. Atapour, X. Wang, M. Persson, I. Odnevall Wallinder, Y.S. Hedberg, Corrosion of binder jetting additively manufactured 316L stainless steel of different surface finish, J. Electrochem. Soc. 167 (13) (2020) 131503.

[53] S.G. Acharyya, A. Khandelwal, V. Kain, A. Kumar, I. Samajdar, Surface working of 304L stainless steel: Impact on microstructure, electrochemical behavior and SCC resistance, Mater. Charact. 72 (2012) 68–76.

[54] F. Scenini, A. Sherry, Stress corrosion cracking of sensitized type 304 stainless steel in high-temperature water with anionic impurities contamination, Corrosion 68 (12) (2012) 1094–1107.

[55] International Atomic Energy Agency, Modelling of transport of radioactive substances in the primary circuit of water-cooled reactors TECDOC-1672. 2012.

[56] J. Mcgrady, The effect of water chemistry on corrosion product build-up under PWR primary coolant conditions, 2016.

[57] T. Terachi, T. Yamada, T. Miyamoto, K. Arioka, K. Fukuya, Corrosion behavior of stainless steels in simulated PWR primary water—effect of chromium content in alloys and dissolved hydrogen, J. Nucl. Sci. Technol. 45 (10) (2008) 975–984.

[58] S. Cissé, L. Laffont, B. Tanguy, M.-C. Lafont, E. Andrieu, Effect of surface preparation on the corrosion of austenitic stainless steel 304L in high temperature steam and simulated PWR primary water, Corros. Sci. 56 (2012) 209–216.

[59] P. Kofstad, High Temperature Corrosion, Elsevier Applied Science, London & New York, 1988.

[60] K. Brunelli, L. Pezzato, E. Napolitani, S. Gross, M. Magrini, M. Dabalà, Influence of atmospheric pressure plasma treatments on the corrosion resistance of stainless steels, Metall. Ital. 106 (7–8) (2014) 35–39.

[61] Y.S. Hedberg, I. Odnevall Wallinder, Metal release from stainless steel in biological environments: a review, Biointerphases 11 (1) (2016) 018901.

[62] Z. Shen, M. Meisnar, K. Arioka, S. Lozano-Perez, Mechanistic understanding of the temperature dependence of crack growth rate in alloy 600 and 316 stainless steel through high-resolution characterization, Acta Mater. 165 (2019) 73–86.

[63] C. Bates, K. Garbett, K. Hinds, G. Lancaster, M. Mantell, G. Renn, Development of corrosion product behaviour and radiation fields at the Sizewell B PWR from 1995 to 2008, VGB Power 88 (12) (2008).

[64] B. Gault, et al., Atom probe tomography, Nat. Rev. Methods Prim. 1 (1) (2021) 51.

[65] K. Thompson, D. Lawrence, D.J. Larson, J.D. Olson, T.F. Kelly, B. Gorman, In situ site-specific specimen preparation for atom probe tomography, Ultramicroscopy 107 (2–3) (2007) 131–139.

[66] J.O. Douglas, P.A.J. Bagot, B.C. Johnson, D.N. Jamieson, M.P. Moody, Optimisation of sample preparation and analysis conditions for atom probe tomography characterisation of low concentration surface species, Semicond. Sci. Technol. 31 (8) (2016) 084004.